Received: 14 February 2023 | Revised: 2 April 2023 | Accepted: 18 April 2023

DOI: 10.1002/cey2.396

RESEARCH ARTICLE

CARBON ENERGY WILEY

Selective photosynthesis of Z-olefins through crystalline metal–organic cage-initiated expeditious cascade reactions

Jia-Ni Lu[1] | Yunze Huang[1] | Yuan-Sheng Xia[1] | Long-Zhang Dong[2] | Lei Zhang[2] | Jing-Jing Liu[2] | Lan-Gui Xie[1] | Jiang Liu[1,2] | Ya-Qian Lan[1,2]

[1]Jiangsu Key Laboratory of New Power Batteries, School of Chemistry and Materials Science, Jiangsu Collaborative Innovation Centre of Biomedical Functional Materials, Nanjing Normal University, Nanjing, China

[2]School of Chemistry, South China Normal University, Guangzhou, China

Correspondence
Jiang Liu and Ya-Qian Lan, Jiangsu Key Laboratory of New Power Batteries, School of Chemistry and Materials Science, Jiangsu Collaborative Innovation Centre of Biomedical Functional Materials, Nanjing Normal University, 210023 Nanjing, China.
Email: liuj@njnu.edu.cn, liuj0828@m.scnu.edu.cn; yqlan@m.scnu.edu.cn and yqlan@njnu.edu.cn

Abstract

The semi-hydrogenation of alkyne to form Z-olefins with high conversion and high selectivity is still a huge challenge in the chemical industry. Moreover, flammable and explosive hydrogen as the common hydrogen source of this reaction increases the cost and danger of industrial production. Herein, we connect the photocatalytic hydrogen evolution reaction and the semi-hydrogenation reaction of alkynes in series and successfully realize the high selective production of Z-alkenes using low-cost, safe, and green water as the proton source. Before the cascade reaction, a series of isomorphic metal–organic cage catalysts ($\mathbf{Co_xZn_{8-x}L_6}$, $x = 0$, 3, 4, 5, and 8) are designed and synthesized to improve the yield of the photocatalytic hydrogen production. Among them, $\mathbf{Co_5Zn_3L_6}$ shows the highest photocatalytic activity, with a H_2 generation rate of 8.81 mmol g^{-1} h^{-1}. Then, $\mathbf{Co_5Zn_3L_6}$ is further applied in the above tandem reaction to efficiently reduce alkynes to Z-alkenes under ambient conditions, which can reach high conversion of >98% and high selectivity of >99%, and maintain original catalytic activity after multiple cycles. This "one-pot" tandem reaction can achieve a highly selective and safe stepwise conversion from water into hydrogen into Z-olefins under mild reaction conditions.

KEYWORDS

alkyne semi-hydrogenation, hydrogen evolution reaction, metal–organic cages, photocatalysis, Z-olefins

1 | INTRODUCTION

The selective hydrogenation of alkynes to produce alkenes is an important basic reaction for the synthesis of fine chemicals, polymer materials, drugs, and fragrances.[1–5] However, in the process of alkyne hydrogenation, there are still two challenges. One is that the adsorption capacity of C=C and C≡C on active metal sites is difficult to distinguish,[6] which makes it difficult to avoid overhydrogenation to generate alkanes.[7] The other is that between the E and Z isomers of alkenes, the synthesis of Z-olefins is more important because it is widely present as a building block in many biologically and pharmaceutically active compounds.[8,9] However, it

is still very difficult to achieve the goal of controllable synthesis of single Z-alkenes owing to their relative thermodynamic instability.[10–12] Currently, Lindlar catalysts ($Pd/CaCO_3$ treated with Pb salts)[13] are commonly used in the industry to catalyze the semi-hydrogenation of alkynes to synthesize Z-olefins. However, this method requires the use of toxic Pb, and produces E-alkene and alkane by-products that reduce the selectivity and yield of Z-alkenes.[14] Therefore, there is an urgent need to develop more efficient and inexpensive catalysts for the highly selective synthesis of Z-alkenes from alkyne semi-hydrogenation.

In addition to the above considerations, a common source of reactant hydrogen for the operation of alkyne semi-hydrogenation is high-pressure hydrogen.[15–18] To ensure the safety of the reaction, investment in equipment related to hydrogen transportation and use is essential, but this will significantly increase the cost of the reaction.[19] To solve this problem, researchers have attempted to use some hydrogen-rich chemicals (e.g., formic acid[20,21] or ammonia borane[22,23]) as the hydrogen source, in situ catalytic release of hydrogen or hydrogen radicals, and then alkyne hydrogenation to reduce the potential hazards of hydrogen usage. However, these chemical feedstocks still have low toxicity and corrosiveness, and the decomposition process is energy-intensive (e.g., heating) and yields undesirable products. As we all know, water is the most abundant proton source on earth, nontoxic, and cheap, and the water-splitting products (H_2 and O_2) are also green. If water is used as the main proton source in the alkyne semi-hydrogenation reaction, that is, the hydrogen evolution reaction and the alkyne semi-hydrogenation reaction are effectively connected in series, it will effectively reduce the cost and toxicity of the reaction and avoid the danger of using hydrogen directly. However, since water molecules are relatively stable at room temperature and pressure ($\Delta G^0 = +237$ kJ/mol), it is difficult to activate and decompose to produce hydrogen.[24] So far, few catalysts have been reported to further reduce the unsaturated bond (C=C, C=O, N=O) by using the H species product generated by green water.[25–27] In particular, the literature of the photocatalytic semi-hydrogenation reaction of alkynes reduced by proton from H_2O is scarce.[28–30]

In this work, we reported the "one-pot" tandem conversion of a photocatalytic hydrogen evolution reaction and an alkyne semi-hydrogenation reaction, which achieved high conversion and selectivity of alkynes to Z-alkenes (Scheme 1). In this tandem reaction, we designed and synthesized a stable, cheap, and efficient metal–organic cage catalyst system, $Co_xZn_{8-x}(OH)_4L_6(H_2O)_2$ (**$Co_xZn_{8-x}L_6$**, $x = 0$, 3, 4, 5, and 8, H_2L=N, N′-(propane-1,3-diyl) bis (1-(1*H*-imidazol-4-yl) methanimine) with different Co/Zn metal ratios, which could catalyze hydrogen production and semi-hydrogenation of the alkyne reaction simultaneously. Among them, **$Co_5Zn_3L_6$** had the best photocatalytic hydrogen evolution activity, and the H_2 production rate was as high as 8.81 mmol g^{-1} h^{-1}. The excellent photocatalytic activity might be attributed to the bimetallic synergistic effect. It was worth noting that under the catalysis of non-noble metal-based **$Co_5Zn_3L_6$**, we successfully achieved the alkyne semi-hydrogenation reaction

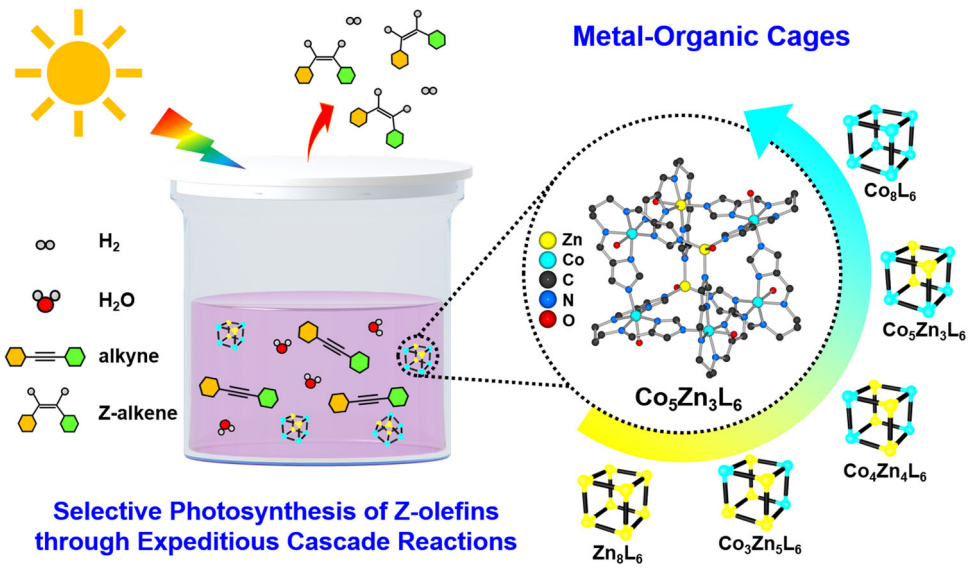

SCHEME 1 One-pot tandem conversion of the photocatalytic hydrogen evolution reaction and the alkyne semi-hydrogenation reaction using metal–organic cages catalysts.

with water as the proton donor. At normal temperature and pressure, alkynes could be converted into Z-alkenes with very high conversion (>98%) and selectivity (>99%). This work shows that photocatalytic hydrogen production and alkyne semi-hydrogenation are connected in series, and the hydrogenation reaction using water as the proton source is successfully realized, avoiding the danger of directly using the hydrogen reactant, reducing the reaction cost, and obtaining the pure product of Z-alkenes, which has excellent potential for industrial application. In addition, through this work, we also found that photostimulation can not only effectively trigger the occurrence of this tandem reaction but also greatly improve the selectivity of Z-alkene products.

2 | EXPERIMENTAL SECTION

2.1 | Synthesis of $Co_xZn_{8-x}L_6$ ($x = 0$, 3, 4, 5, and 8)

H_2L (0.04 mmol) and $CoCl_2{\cdot}6H_2O$ (0.08 mmol) were dissolved in a mixture solution of dimethylformamide (DMF) (4 mL), H_2O (1 mL), and MeOH (1 mL) by ultrasonication, and then a drop of HNO_3 was added. Subsequently, the mixture solution was transferred to a 10 mL glass vial for 72 h at 100°C under autogenous pressure. After cooling down to room temperature, dark red cubic-shaped crystals ($\mathbf{Co_8L_6}$) were collected by filtration and washed with DMF and MeOH (Yield: 78%). $\mathbf{Co_xZn_{8-x}L_6}$ ($x = 0$, 3, 4, and 5) was prepared using a similar method, except for the use of metal salt, detailed in the Supporting Information.

2.2 | Photocatalytic H_2 evolution experiments

Photocatalytic H_2 production experiments were performed in a sealed 50 mL Pyrex flask. A 300 W Xe lamp with a wavelength range from 300 to 1100 nm was used as the light source to trigger the photocatalytic reaction. The reaction temperature was controlled at 25°C by using cooling water circulation. In a typical experiment, the catalyst (5 mg) was added to the mixed solution, which consisted of MeCN/H_2O (30 mL, vol/vol = 14:1), ascorbic acid (0.1 mol/L) as an electron donor, and $[Ru(bpy)_3]Cl_2{\cdot}6H_2O$ (bpy = 2′,2-bipyridine, 10 mg) as a photosensitizer. Before irradiation, the system was degassed with Ar to remove dissolved O_2 for 30 min. To detect the formation of hydrogen from the reaction mixture, 500 μL from the middle of the reactor was taken out with a syringe and injected into a gas chromatography (GC) with a thermal conductivity detector (TCD) using nitrogen as the carrier gas and the reference gas. All glassware was carefully rinsed with ultrapure water before usage. Photocatalytic stability tests were performed using the same processing parameters.

2.3 | Photocatalytic tandem reaction experiments

For a better comparison, all organic measurements were carried out under equivalent experimental conditions. To achieve high gas density in the reaction volume, the relatively small volume of the chamber reactor (25 mL Schlenk tube) was selected. In a typical procedure, 5 mg of catalysts, 0.1 mmol of alkynes, 2 mL of ultrapure water, 8 mL of MeCN, 0.1 mol/L of ascorbic acid, and 10 mg of $[Ru(bpy)_3]Cl_2{\cdot}6H_2O$ were first added; then, the reactor was sealed and purged with Ar for 30 min. Afterwards, the reactor was irradiated by a 300 W Xe lamp with a wavelength range from 300 to 1100 nm at 25°C. The H_2 produced was determined by GC using a thermal conductivity detector (TCD) detector. The hydrogenation products were detected and quantified by gas chromatography-mass spectrometry (GC–MS) and nuclear magnetic resonance (NMR) analyses after purification by column chromatography on a silica gel.

3 | RESULTS AND DISCUSSION

3.1 | Structure and characterization

It is well known that crystalline coordination compounds have well-defined crystal structures, and specific structures can be designed by functionalizing organic linkers or modulating components.[31–35] Metal–organic cages (MOCs), as one of the crystalline complexes, are discrete molecules that self-assemble from organic linkers and metal ions or clusters.[36,37] MOCs contain independent cavities that can act as nanoreactors with potential applications in various fields such as adsorption separation,[38,39] host–guest chemistry,[40–42] and catalysis.[43–45] Herein, we designed and synthesized a series of isostructural monometallic–organic cages ($\mathbf{Zn_8L_6}$ and $\mathbf{Co_8L_6}$) and bimetallic–organic cages ($\mathbf{Co_xZn_{8-x}L_6}$, $x = 3$, 4, and 5; Figure 1). The crystal structure is described by taking $\mathbf{Co_8L_6}$ as an example. Single-crystal X-ray diffraction analysis reveals that $\mathbf{Co_8L_6}$ crystallizes in the rhombohedral space group *R-3* with an asymmetric unit consisting of two cobalt ions, one ligand, one water molecule, and one hydroxide ion (Figure S2). $\mathbf{Co_8L_6}$ has

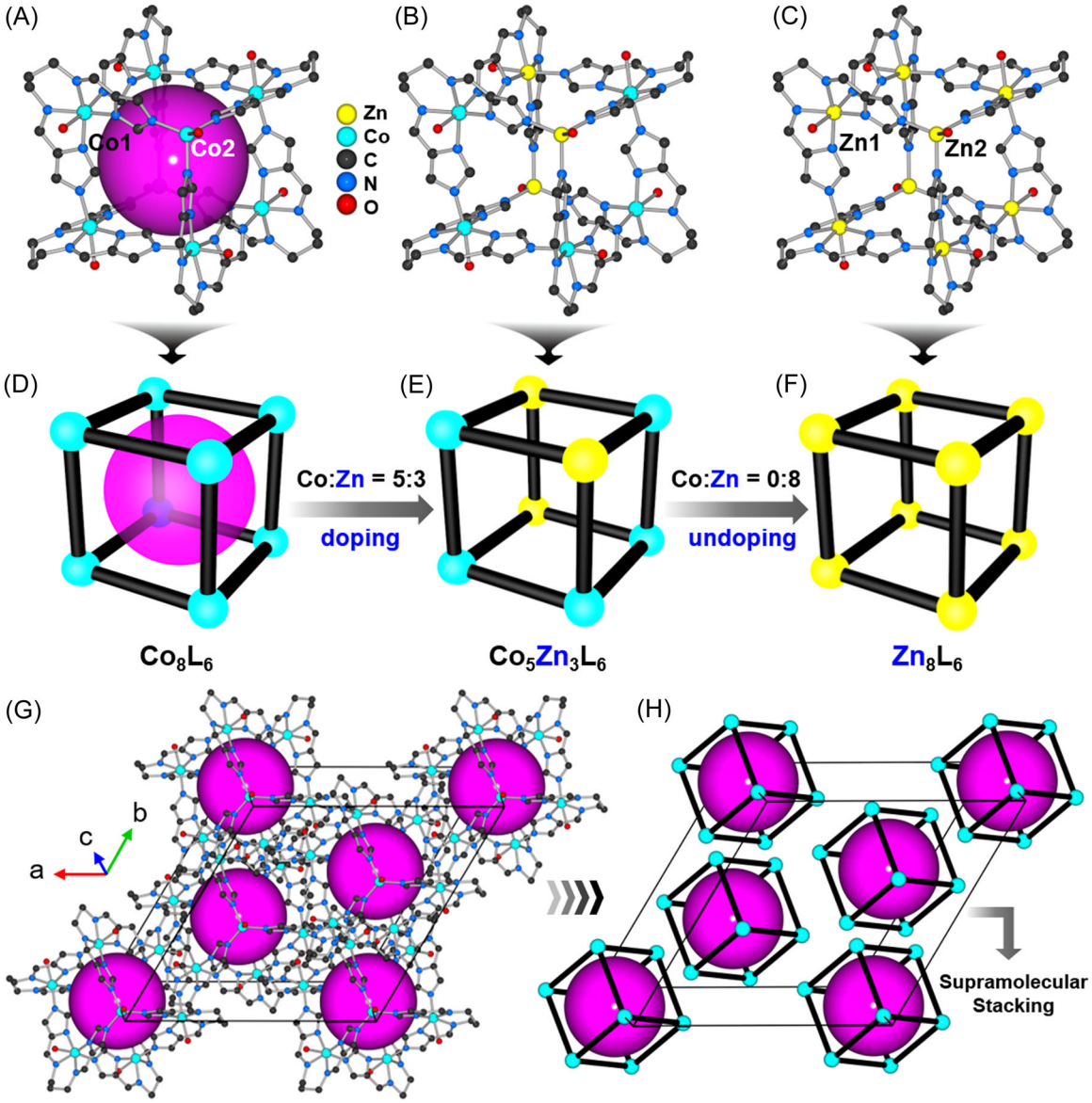

FIGURE 1 Crystal structures of (A) $\mathbf{Co_8L_6}$, (B) $\mathbf{Co_5Zn_3L_6}$, and (C) $\mathbf{Zn_8L_6}$. Schematic diagram of the crystal structure of (D) $\mathbf{Co_8L_6}$, (E) $\mathbf{Co_5Zn_3L_6}$, and (F) $\mathbf{Zn_8L_6}$. (G) Three-dimensional (3D) supramolecular stacking diagram of $\mathbf{Co_8L_6}$ and (H) schematic diagram of the 3D stacking diagram of $\mathbf{Co_8L_6}$.

an 8-nucleus distorted cubic structure and contains two types of geometrically independent cobalt ions (Co1 and Co2). Co1 is octahedral coordinated, which is chelated by four N atoms from one ligand and binds one imidazole N atom from another ligand and a OH^- or a H_2O (Figure 4). Co2 is a tetrahedral coordination center that coordinates with three ligands by imidazolium N atoms and a OH^- (Figure S3B). The four N atoms in the center of each ligand chelate a Co1 ion, and the two imidazole N atoms of the ligand are linked to a pair of Co1 and Co2 ions. Through the above connection method, six Co1 ions, two Co2 ions, and six ligands form a cubic cage, and the cavity diameter of the cage is about 6.13 Å. Interaction of adjacent cages with each other occurs by hydrogen bonds, eventually forming a three-dimensional supramolecular compound (Figure S4). Remarkably, by simply replacing Co ions with Zn ions of similar radii in the synthesis, we can also construct isostructural $\mathbf{Zn_8L_6}$. Moreover, a series of bimetallic–organic cages, $\mathbf{Co_xZn_{8-x}L_6}$ ($x = 3$, 4, and 5), can be synthesized by systematically tuning the Co/Zn ion ratio.

As shown in Figure S5, the powder X-ray diffraction (PXRD) patterns of $\mathbf{Co_xZn_{8-x}L_6}$ ($x = 0$, 3, 4, 5, and 8) were very consistent with the simulated peaks, which proved their high crystallinity and purity, and further demonstrated that they had a similar structure. In addition, all of them shared similar Fourier-transform infrared peaks (Figure S6), which indicated that they

were isostructural. In detail, the peaks at around 2931, 2848, 1670, 1628, and 1112 cm^{-1} were the antisymmetric and symmetric stretching vibration peaks of CH_2, the stretching vibration peak of C=C, the C=N absorbance band, and the stretching vibration peak of C–N. Through an optical microscope (Figure S7A–E), we could clearly observe that metal–organic cages ($\mathbf{Co_xZn_{8-x}L_6}$, $x = 0$, 3, 4, 5, and 8) were cubic crystals, but their crystal colors changed with the ratio of Co/Zn in the crystal lattice. As the Co/Zn ratio changed regularly from 0:8, 3:5, 4:4, 5:3 to 8:0, the color of the crystals also deepened significantly, from colorless to brown to dark red. Their morphologies and sizes were further characterized by scanning electron microscopy (SEM) images (Figure S7F–O). Obviously, $\mathbf{Co_xZn_{8-x}L_6}$ ($x = 0$, 3, 4, 5, and 8) were regular cubic single crystals of uniform size with an average side length of 10–20 μm. The SEM-energy-dispersive X-ray spectroscopy (EDS) elemental mapping images of $\mathbf{Co_xZn_{8-x}L_6}$ ($x = 0$, 3, 4, 5, and 8) revealed a uniform distribution of Co or Zn elements in the crystals, demonstrating the even doping of Co and Zn in the crystals (Figure S7P–Y). The basic composition and the molar ratios of Co/Zn of these cages could be further evaluated by EDS. It was observed from the EDS spectra (Figures S8–S12) that $\mathbf{Zn_8L_6}$ consisted of Zn, C, N, and O, $\mathbf{Co_xZn_{8-x}L_6}$ ($x = 3$, 4, and 5) consisted of Zn, Co, C, N, and O, and $\mathbf{Co_8L_6}$ consisted of Co, C, N, and O. Besides, according to EDS, the atomic ratios of Co and Zn for $\mathbf{Co_xZn_{8-x}L_6}$ ($x = 3$, 4, and 5) were 1:1.70, 1:1.04, and 1:0.69, respectively (Table S4). Inductively coupled plasma emission spectroscopy showed that the stoichiometries of Co/Zn in $\mathbf{Co_xZn_{8-x}L_6}$ ($x = 3$, 4, and 5) were 1:1.78, 1:0.97, and 1:0.55, respectively (Table S5), which corresponds to the EDS results.

To determine the positional distribution of Co and Zn ions in the bimetallic–organic cage structure, we simulated the energy of $\mathbf{Co_7ZnL_6}$ by density functional theory (DFT) calculations. $\mathbf{Co_7ZnL_6}$ had the possibility of two metal distributions, that is, Zn substituted for Co1 or Co2. The calculation results showed that the structural energy of four-coordinated Zn (the Co2 site was substituted by Zn; Figure S13B) was 0.96 eV lower than that of six-coordinated Zn (the Co1 site was substituted by Zn; Figure S13A), and the structure was more stable. Therefore, Zn preferentially occupied four-coordinated sites in bimetallic–organic cages.

Meanwhile, thermogravimetric analyses showed that the structures of $\mathbf{Co_xZn_{8-x}L_6}$ were stable until about 300°C (Figures S14–S18). Elements present in $\mathbf{Co_xZn_{8-x}L_6}$ and their corresponding valence states were characterized by X-ray photoelectron spectroscopy (XPS). The XPS survey patterns (Figure S19) proved that $\mathbf{Co_xZn_{8-x}L_6}$ all consisted of C, N, O. In addition, $\mathbf{Co_xZn_{8-x}L_6}$ ($x = 0$, 3, 4, and 5) consisted of Zn and the content of Zn gradually decreased, while $\mathbf{Co_xZn_{8-x}L_6}$ ($x = 3$, 4, 5, and 8) consisted of Co and the content of Co gradually increased. As shown in Figure S20A, for $\mathbf{Zn_8L_6}$, the XPS Zn $2p_{3/2}$ peak located at 1021.23 eV and the $2p_{1/2}$ peak located at 1044.31 eV, indicating that Zn only had an oxidation state of +2. Figure S21D shows that binding energies at 781.44 eV (Co $2p_{3/2}$) and 796.58 eV (Co $2p_{1/2}$) belonged to the Co(II) ion in $\mathbf{Co_8L_6}$. Similarly, all Zn and Co ions of $\mathbf{Co_xZn_{8-x}L_6}$ ($x = 3$, 4, and 5) were divalent (Figures S20 and S21).

Because the crystals of $\mathbf{Co_xZn_{8-x}L_6}$ ($x = 0$, 3, 4, 5, and 8) had different shades of colors, solid-state ultraviolet-visible-near-infrared diffuse reflectance spectroscopy (UV/Vis-NIR DRS) was carried out to detect their light absorption capacity. Figure 2A shows that colorless $\mathbf{Zn_8L_6}$ had strong light absorption in the UV region at around 310 nm, but only weak absorption in the visible light region and the infrared light region. By contrast, dark red $\mathbf{Co_8L_6}$ showed a broad UV/Vis-NIR absorption region from 300 to 1500 nm. Therefore, brown $\mathbf{Co_xZn_{8-x}L_6}$ ($x = 3$, 4, and 5) obtained by doping Co into $\mathbf{Zn_8L_6}$ enhanced the absorbance of visible and infrared light, which was slightly weaker than $\mathbf{Co_8L_6}$. This means that the electrons of $\mathbf{Co_xZn_{8-x}L_6}$ ($x = 3$, 4, 5, and 8) with Co were more easily excited under visible light and infrared light irradiation those that of $\mathbf{Zn_8L_6}$ only with Zn. These better light harvesting abilities were due to charge transfer between the ligand and the metal ion. The optical band gap (E_g) values of $\mathbf{Co_xZn_{8-x}L_6}$ ($x = 0$, 3, 4, 5, and 8) were calculated to be 3.06 eV ($\mathbf{Zn_8L_6}$), 2.23 eV ($\mathbf{Co_3Zn_5L_6}$), 1.91 eV ($\mathbf{Co_4Zn_4L_6}$), 1.89 eV ($\mathbf{Co_5Zn_3L_6}$), and 1.87 eV ($\mathbf{Co_8L_6}$) by the Kubelka–Munk function (Figures S22–S26), unveiling their potential for use as semiconducting catalysts. Mott–Schottky measurements were performed to determine the lowest unoccupied molecular orbital (LUMO) position of these cages. The final LUMO positions of $\mathbf{Co_xZn_{8-x}L_6}$ ($x = 0$, 3, 4, 5, and 8) were estimated to be −1.25, −0.67, −0.65, −0.60, and −0.71 V vs. normal hydrogen electrode (NHE, pH 7), respectively (Figures S27–S31). By performing UV/Vis-NIR DRS associated with Mott–Schottky measurements, the highest occupied molecular orbital (HOMO) positions of $\mathbf{Co_xZn_{8-x}L_6}$ ($x = 0$, 3, 4, 5, and 8) were calculated to be 1.81, 1.56, 1.26, 1.29, and 1.16 V (vs. NHE, pH 7), respectively (Figure 2B). To verify the accuracy of above results, the HOMO positions of $\mathbf{Co_xZn_{8-x}L_6}$ ($x = 0$, 3, 4, 5, and 8) were determined by UV photoelectron spectroscopy (Figures S32–S36), from which the HOMO positions were calculated to be −6.65, −6.43, −6.11, −6.15, and −6.02 eV (vs. vacuum level, E_v), respectively. Simultaneously, the HOMO energy levels of $\mathbf{Co_xZn_{8-x}L_6}$ ($x = 0$, 3, 4, 5, and 8) were calculated to be 1.80, 1.58, 1.26, 1.30, and 1.17 V (vs. NHE, pH 7), respectively, which

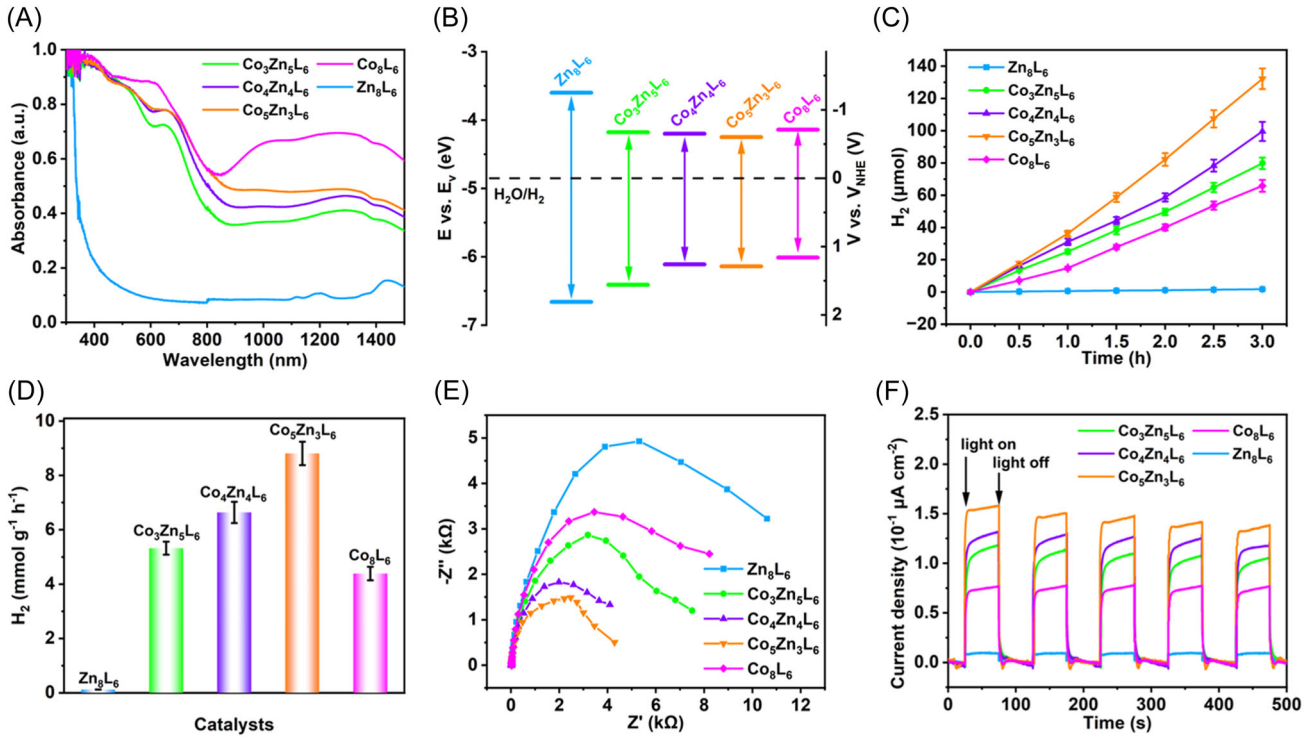

FIGURE 2 (A) UV/Vis spectra of $\mathbf{Co_xZn_{8-x}L_6}$ ($x = 0$, 3, 4, 5, and 8). (B) Band structure for $\mathbf{Co_xZn_{8-x}L_6}$. (C) H_2 yield of $\mathbf{Co_xZn_{8-x}L_6}$. (D) H_2 evolution rate of $\mathbf{Co_xZn_{8-x}L_6}$. (E) EIS Nyquist plots of $\mathbf{Co_xZn_{8-x}L_6}$. (F) Transient photocurrent responses of $\mathbf{Co_xZn_{8-x}L_6}$.

were in agreement with the values obtained from Mott–Schottky measurements and UV/Vis-NIR DRS. Obviously, as shown in Figure 2B, the LUMO positions of these cages were more negative than the redox potential of H_2/H_2O (4.85 eV vs. E_v, 0 V vs. NHE, pH 7). Therefore, theoretically, these cages could serve as efficient catalysts for hydrogen production due to the matching of their band structure.

3.2 | Photocatalytic hydrogen evolution performance

Based on the broad absorption range, enhanced charge-transfer rate, and more negative LUMO sites, $\mathbf{Co_xZn_{8-x}L_6}$ ($x = 0$, 3, 4, 5, and 8) has potential for use as an excellent catalyst for photocatalytic hydrogen evolution. To test the photocatalytic hydrogen evolution performances of these cages, the photocatalytic reaction was carried out in an Ar-saturated MeCN/H_2O solvent with ascorbic acid as a sacrificial agent and $[Ru(bpy)_3]Cl_2{\cdot}6H_2O$ (bpy = 2′,2-bipyridine) as a photosensitizer under UV/Vis-NIR light. At first, monometallic–organic cages ($\mathbf{Zn_8L_6}$ and $\mathbf{Co_8L_6}$) were used as catalysts. Figure 2C,D shows that the hydrogen evolution rate (4.39 mmol g^{-1} h^{-1}) of $\mathbf{Co_8L_6}$ was slightly higher than that of $\mathbf{Zn_8L_6}$ (0.12 mmol g^{-1} h^{-1}) under the same conditions, probably because Co sites of $\mathbf{Co_8L_6}$ could act as both catalytic sites and cocatalytic sites, which was more active than Zn. After Co/Zn doping, the catalytic performance of $\mathbf{Co_xZn_{8-x}L_6}$ ($x = 3$, 4, and 5) significantly improved, and the H_2 generation rates were 5.32, 6.64, and 8.81 mmol g^{-1} h^{-1}, respectively. Meanwhile, the turnover number (TON) was one of the most important indexes for evaluation of the catalytic activity. As listed in Table S6, the TONs of $\mathbf{Co_xZn_{8-x}L_6}$ ($x = 0$, 3, 4, 5, and 8) were 0.70, 32.13, 39.97, 52.87, and 26.08, respectively. It is reported that Co-based materials are commonly used cocatalysts in photocatalytic reactions.[46,47] Therefore, the reason for the better performance of $\mathbf{Co_xZn_{8-x}L_6}$ ($x = 3$, 4, and 5) may also be that the catalytic sites (Zn sites and Co sites) and the cocatalytic sites (Co sites) are concentrated on the same cage, and the two types of sites are connected by ligands to form electron transport channels, which enhance their synergistic effect. The catalytic performance of bimetallic cages with any Co/Zn ratio is much higher than that of monometallic cages ($\mathbf{Zn_8L_6}$ and $\mathbf{Co_8L_6}$), fully demonstrating that the bimetallic synergistic effect can greatly improve the catalytic performance. Notably, the H_2 generation rate of the best-performing $\mathbf{Co_5Zn_3L_6}$ was 73.42 times and 2.01 times higher than that of $\mathbf{Zn_8L_6}$ and $\mathbf{Co_8L_6}$, respectively. Taking $\mathbf{Co_5Zn_3L_6}$ as an example, we evaluated the influence of different masses of catalysts on the H_2 yield

and the production rate of the hydrogen evolution reaction. As shown in Figure S38, it could be concluded that as the mass increased, the H_2 yield gradually increased, but the production rate decreased. Considering the actual experimental conditions, the reason for this result was not only linked to the light scattering effect but also the effective contact area between the catalyst and light irradiation.

The charge separation efficiency was one of the important factors affecting the photocatalytic performance. To explore the role of bimetallic synergy in charge separation, we carried out electrochemical impedance spectroscopy (EIS) and transient short-circuit photocurrent response tests of $\mathbf{Co_xZn_{8-x}L_6}$ ($x = 0$, 3, 4, 5, and 8). Compared with monometallic catalysts, the synergistic effect of Zn and Co doping may reduce the impedance of materials. In fact, $\mathbf{Co_xZn_{8-x}L_6}$ ($x = 3$, 4, and 5) showed a smaller Nyquist curve semicircle diameter compared to $\mathbf{Zn_8L_6}$ and $\mathbf{Co_8L_6}$ in the EIS measurements, implying that the order of charge transport rates of cages was $\mathbf{Co_5Zn_3L_6} > \mathbf{Co_4Zn_4L_6} > \mathbf{Co_3Zn_5L_6} > \mathbf{Co_8L_6} > \mathbf{Zn_8L_6}$ (Figure 2E). This indicated that lower interfacial charge-transfer resistance and higher electronic conductivity could be obtained by uniformly doping Zn and Co in the cage. As a proof of concept, transient short-circuit photocurrent response tests (Figure 2F) were performed to explore the efficiency of photoinduced electron transfer. When the light was turned on, the photocurrent was rapidly generated and then remained stable. The photocurrent decayed rapidly when the light was turned off, indicating that all cages had strong photocurrent responses. It was worth noting that the transient photocurrent response intensities of $\mathbf{Co_5Zn_3L_6}$ were 1.23, 1.37, 2.09, and 15.65 times higher than those of $\mathbf{Co_4Zn_4L_6}$, $\mathbf{Co_3Zn_5L_6}$, $\mathbf{Co_8L_6}$, and $\mathbf{Zn_8L_6}$, respectively. Thus, the Co/Zn synergy enhanced the separation efficiency of photogenerated electrons and holes, prevented electron–hole recombination, and increased the surface photogenerated electron density of the catalyst, thereby dynamically accelerating the rate of the electron reduction reaction and hydrogen production.

In addition, the change of photocatalytic activity might be related to the electronic state of the metal. As shown in the XPS Co 2p spectra (Figure S21), compared with $\mathbf{Co_8L_6}$, the binding energies for Co 2p in bimetal–organic cages decreased, and the order of the binding energy for Co 2p was $\mathbf{Co_8L_6} > \mathbf{Co_3Zn_5L_6} > \mathbf{Co_4Zn_4L_6} > \mathbf{Co_5Zn_3L_6}$. Correspondingly, the binding energies of Zn 2p in the bimetallic–organic cages increased compared to $\mathbf{Zn_8L_6}$, and the degree of migration was $\mathbf{Co_5Zn_3L_6} > \mathbf{Co_4Zn_4L_6} > \mathbf{Co_3Zn_5L_6}$ (Figure S20). This indicated that after Co/Zn doping, some of the electrons of Zn were transferred to Co, resulting in an increase in the electron density of Co, improving the reducibility of Co. In a word, Co/Zn doping regulated the electronic structure of Co, improved its reducibility, and enhanced its catalytic activity, thereby increasing the hydrogen evolution rate.

To fully evaluate the catalytic activity of $\mathbf{Co_5Zn_3L_6}$, we performed a series of control experiments. H_2 was not detected by GC when the reaction was run in the absence of light, ascorbic acid, $[Ru(bpy)_3]Cl_2{\cdot}6H_2O$, or H_2O (Table S8, entries 1–4). When the tests were carried out under no MeCN or $\mathbf{Co_5Zn_3L_6}$, only trace amounts of hydrogen could be detected (Table S8, entries 5–6). If any one factor was removed, the catalytic performance decreased sharply, which proved that the above factors were indispensable in the photocatalytic process.

The durability of the catalyst is an important indicator when evaluating the quality of a catalyst. Taking the superior performance of $\mathbf{Co_5Zn_3L_6}$ as an example, the production of H_2 was almost unchanged after three cycles of experiments (Figure S39). PXRD results of $\mathbf{Co_xZn_{8-x}L_6}$ ($x = 0$, 3, 4, 5, and 8) before and after the reaction were consistent, proving that the catalysts remained stable during the reaction (Figure S40). The metal ion contents of the solutions after the reactions were detected by inductively coupled plasma atomic emission spectroscopy (Table S9), and the results showed that zinc and cobalt ions were not detected, which further confirmed the stability of the heterogeneous catalysts in the reaction system.

3.3 | Mechanism of photocatalytic hydrogen evolution

To determine the structure–property relationship, DFT calculations were performed based on explicit crystal structure models. We compared the free-energy changes of the two catalytically active sites (tetrahedral sites and octahedral sites) in the monometallic–organic cages ($\mathbf{Co_8L_6}$ and $\mathbf{Zn_8L_6}$) for photocatalytic hydrogen evolution (Figure 3A). In the hydrogen evolution reaction, the rate-determining step was the formation of *H (Symbol * represents the active site for adsorption and reaction). For $\mathbf{Co_8L_6}$, the octahedral Co site had a free-energy activation barrier (ΔG) of −0.20 eV, which was much smaller than that of the tetrahedral Co site ($\Delta G = 0.59$ eV). Meanwhile, the ΔG of the tetrahedral Zn site (2.57 eV) was also larger than that of the octahedral Zn site (2.37 eV) in $\mathbf{Zn_8L_6}$. Therefore, the main catalytically active sites in monometallic–organic cages were the octahedral coordinated metal sites. At the same time, the free-energy barrier of the Zn site was

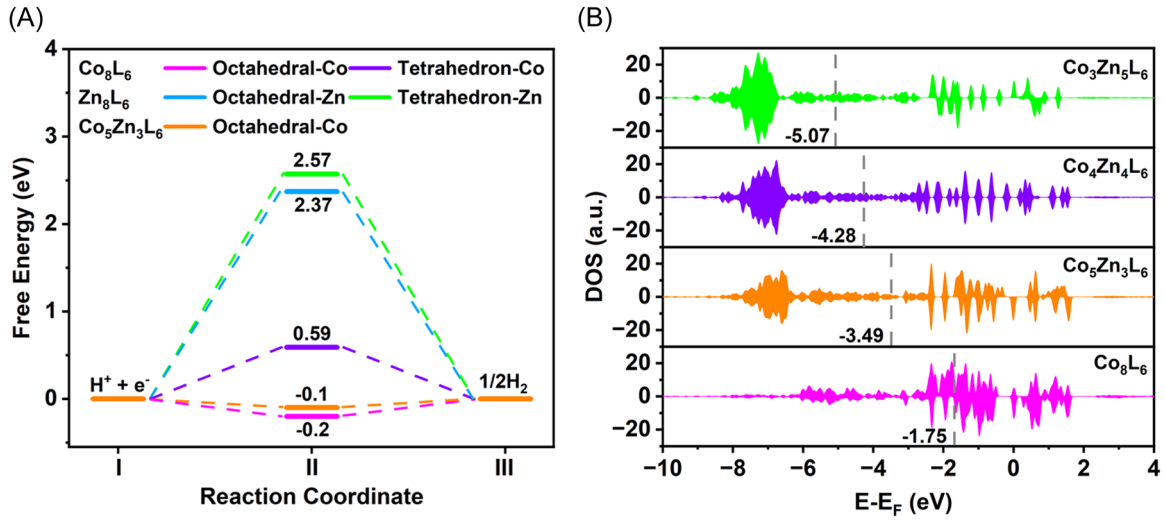

FIGURE 3 (A) Calculated free-energy diagram for photocatalytic H_2 production over $\mathbf{Co_xZn_{8-x}L_6}$ ($x = 0$, 5, and 8). (B) Density of states (DOS) on the d-band of Co active sites in $\mathbf{Co_xZn_{8-x}L_6}$ ($x = 3$, 4, 5, and 8) catalysts.

much higher than that of the Co site whether it was a six-coordination site or a four-coordination site. Based on the above information, in the bimetallic–organic cage ($\mathbf{Co_xZn_{8-x}L_6}$, $x = 3$, 4, and 5), the octahedral Co sites were the main catalytic sites for photocatalytic hydrogen evolution. Taking $\mathbf{Co_5Zn_3L_6}$ as a representative of bimetallic–organic cages, the octahedral Co site of $\mathbf{Co_5Zn_3L_6}$ had the lowest free-energy activation barrier of −0.10 eV, which was consistent with the experimental results showing that its catalytic performance
for hydrogen evolution was better than that of monometallic–organic cages.

To study the adsorption capacity of catalysts and reaction intermediates (*H), the density of states on the d-band of Co active sites in $\mathbf{Co_xZn_{8-x}L_6}$ ($x = 3$, 4, 5, and 8) catalysts were calculated and are shown in Figure 3B. The Fermi level in the calculation was set as 0 eV. When the Co/Zn atomic ratios of bimetallic–organic cages were 3:5, 4:4, and 5:3, the d-band centers were −5.07, −4.28, and −3.49 eV, respectively, which indicated that the d-band states shifted towards the Fermi energy level (E_F). In general, the closer the d-band center of the transition metal to the Fermi level, the higher the catalytic activity,[48] resulting in stronger adsorption of metal active sites to *H. Hence, the order of the catalytic activity of bimetallic–organic cages was $\mathbf{Co_5Zn_3L_6 > Co_4Zn_4L_6 > Co_3Zn_5L_6}$, which was in agreement with the experimental results. The d-band center of $\mathbf{Co_8L_6}$ (−1.75 eV) was closer to the Fermi level than that of bimetallic–organic cages, but the catalytic performance was indeed lower than that of $\mathbf{Co_xZn_{8-x}L_6}$ ($x = 3$, 4, and 5), probably because the Co active sites in $\mathbf{Co_8L_6}$ were too strongly adsorbed to *H, which was not conducive to H_2 release.

To study the electron transport mode during photocatalytic hydrogen evolution, an UV-Vis absorption spectrum experiment of $[Ru(bpy)_3]Cl_2$ (PS) was performed (Figure S41). In the absence of a catalyst, PS was rapidly bleached after illumination because the $PS^{\bullet-}$ state generated during photogenerated electron transfer was unstable. Obviously, the bleaching of PS became slower under the same illumination time after adding the catalyst, indicating that the photogenerated electrons were transferred from PS to the catalyst, extending the PS lifetime. Based on the above considerations, the possible mechanism of hydrogen evolution is shown in Figure S42. First, the OH^- on the six-coordinated Co^{II} site scattered to generate Co^{II} with an active site, which was reduced to Co^{I} by the photogenerated electrons transferred from PS. Co^{I} combined with a proton from H_2O to form Co^{III}–H, and gained another proton in solution to release H_2, returning to the original Co^{II}.

3.4 | Photocatalytic tandem reaction performance

For hydrogenation reduction reactions, the storage and transportation of H_2 are costly and involve certain risks.[49] Hence, we hope to utilize the proton from water for the one-pot tandem catalytic reaction for further synthesis of valuable organics. This method can not only efficiently and directly utilize the in situ-generated H species, avoiding the dangers of using hydrogen, but also obtain high-value organic chemical pure products. This may

represent an avenue for photocatalytic hydrogen production for practical applications in industry in the future. The one-pot method is more conducive to the transfer of protons from water molecules to organic substrates, but it is more difficult to achieve the conditions of hydrogen production and organic reactions at the same time.[50] Based on the above considerations, we chose to carry out the hydrogen evolution and semi-hydrogenation of alkyne reactions in series. To explore the best reaction conditions, several control experiments using diphenylacetylene as a model substrate and **$Co_5Zn_3L_6$** as a hydrogen evolution catalyst were performed. Hydrogen gas was analyzed by GC, and alkyne conversion and alkene selectivity were determined by GC–MS.

It is well known that solvents often play a crucial role in the conversion and selectivity of organic reactions.[51,52] Hence, Figure 4B shows the influence of solvents on the photocatalytic tandem reaction. Compared with acetonitrile, which had a certain toxicity, we preferred to complete the reaction in pure water. Unfortunately, the yield of active H species under pure water conditions was too low, and diphenylacetylene was insoluble in water, reducing the contact of H species with diphenylacetylene, so almost no hydrogenation product was produced (Table S10, entry 1). Meanwhile, pure acetonitrile could not produce H species, so diphenylacetylene did not undergo hydrogenation reduction (Table S10, entry 5). Because acetonitrile could improve the solubility of diphenylacetylene, and water was the proton source, we chose a mixed solvent of acetonitrile and water for the tandem reaction. When the volume ratio of MeCN/H_2O was 1:4 (Table S10, entry 2), H_2 production was 8.30 μmol, and a small amount of diphenylacetylene with a conversion of 15% was reduced to *cis*-stilbene (selectivity = 79%). Also, a H_2 output of 8.35 μmol, a conversion of 80%, and a selectivity of 91% for *cis*-stilbene were obtained under the conditions of MeCN/H_2O = 1:1 (Table S10, entry 3). The best mixed solvent was MeCN/H_2O = 4:1, and 12.82 μmol H_2 was produced and further reduced diphenylacetylene to *cis*-stilbene, whose yield and selectivity were as high as 98% and 99%, respectively - (Figure S44 and Table S10, entry 4). Owing to the increased H species production and enhanced substrate solubility, diphenylacetylene was almost completely converted into *cis*-stilbene rather than *trans*-stilbene and 1,2-diphenylethane under ambient temperature and pressure within 3 h. Among the reported catalysts for the semi-hydrogenation of alkynes, most of them required higher temperature and high hydrogen pressure for efficient completion of the reaction (Table S11). Surprisingly, using an one-pot method, diphenylacetylene could be directly reduced to *cis*-stilbene by photocatalytically generated active H species without additional heating and pressure. In this way, the energy consumption and cost of the reaction were greatly reduced, which is beneficial for subsequent applications in industry.

The semi-hydrogenation of alkynes cannot proceed spontaneously under ambient conditions without catalysts. However, in this one-pot reaction, without the addition of a specific catalyst, the alkyne realizes the semi-hydrogenation reaction. Therefore, we investigated whether the various components in the reaction system could catalyze the semi-hydrogenation of alkynes. In Table S12, entries 2–4 show that ascorbic acid, $[Ru(bpy)_3]Cl_2{\cdot}6H_2O$, and **$Co_5Zn_3L_6$** cannot catalyze the hydrogenation reduction of diphenylacetylene with an additional H_2 balloon under light. As a result, we speculated that diphenylacetylene was directly and spontaneously reduced by the H species generated by water, rather than reacting with the final combined H_2. As a proof of concept, we performed isotope labeling control experiments using D_2O instead of H_2O to explore the proton source for hydrogenation, and the corresponding products were detected by GC–MS. When H_2O was used (Figure 4D), the *m*/*z* value of 179.1 was assigned to the fragmentation ion *cis*-stilbene radical. When H_2O was replaced with D_2O, this signal peak shifted to 181.1, which was the same result as that using both D_2O and a H_2 balloon. Meanwhile, the results of ^1H NMR (Figures S45–S47) and high-resolution mass spectrometry (Figures S48–S50) were in good agreement with that of GC–MS. In addition, ^1H NMR spectra (Figure S51) of the liquid phase from the photocatalytic semi-hydrogenation of diphenylacetylene further confirmed this point. These experiments fully demonstrated that diphenylacetylene was reduced by in situ-generated protons from water, independent of H_2.

To further investigate the reason why the product of the semi-hydrogenation of diphenylacetylene was *cis*-stilbene instead of *trans*-stilbene, we replaced diphenylacetylene with *trans*-stilbene and performed experiments under the same conditions. From Table S13, entries 1–4, it is clear that *trans*-stilbene could not be converted into *cis*-stilbene under dark conditions with or without the addition of ascorbic acid, $[Ru(bpy)_3]Cl_2{\cdot}6H_2O$, or **$Co_5Zn_3L_6$**. This transformation could occur under light with the conversion of 47% (Table S13, entry 5). However, with the addition of ascorbic acid, $[Ru(bpy)_3]Cl_2{\cdot}6H_2O$, or **$Co_5Zn_3L_6$**, the conversion increased slightly (Table S13, entries 6–8). Therefore, illumination was the decisive factor for the conformational transformation. To study the effect of light on the conversion of *cis*–*trans* isomers, we tested the changes of *trans*-stilbene under different wavelength ranges of light. Interestingly, when irradiated under UV light (Table S13, entry 9) and

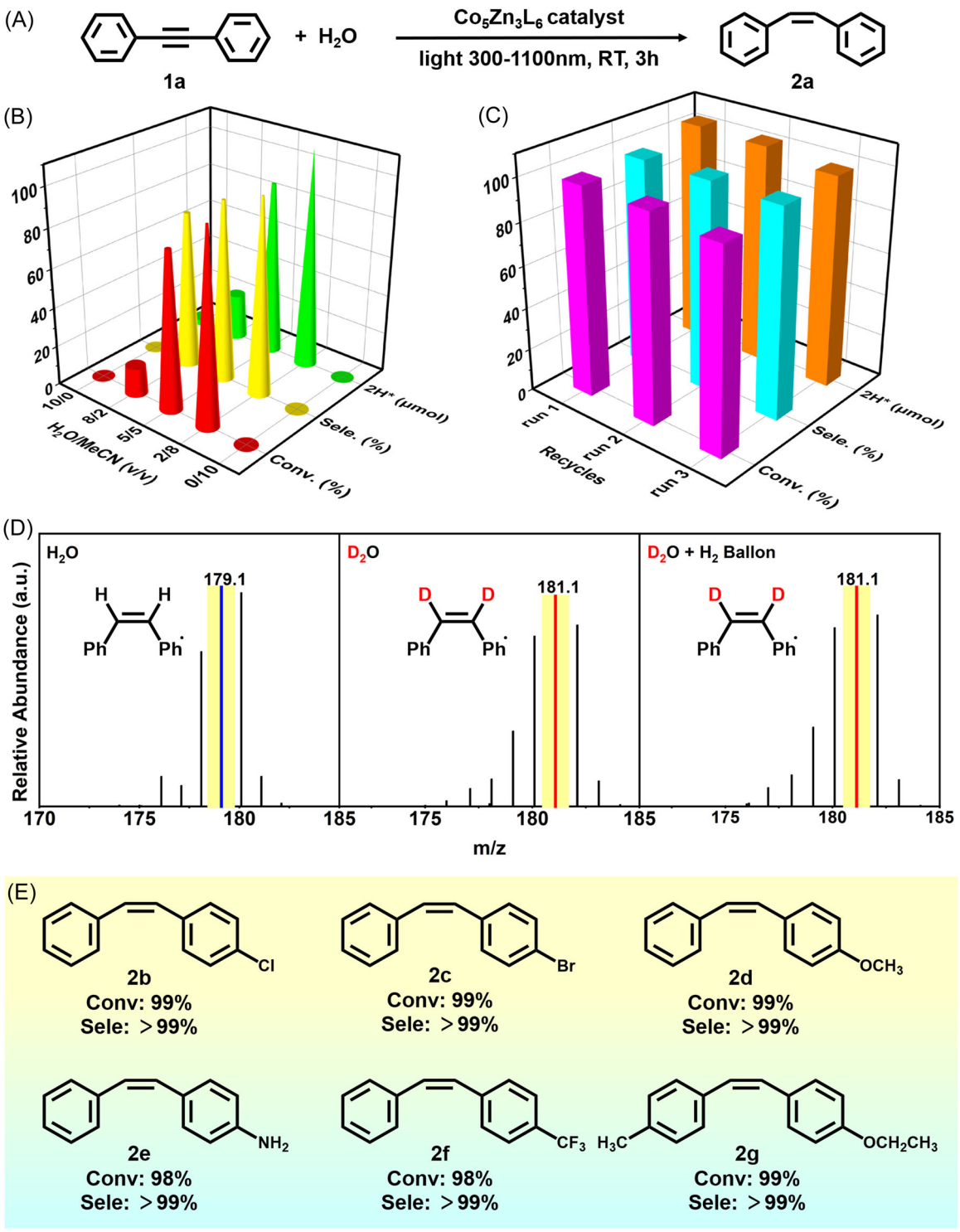

FIGURE 4 (A) Schematic illustration of the synthesis procedure of *cis*-stilbene via a tandem reaction using H_2O as the proton source. (B) Conversion, selectivity, and H_2 yield of the tandem reaction in different mixed solvents. (C) Recycle experiments of the tandem reaction. (D) Different mass charge ratios (m/z) using H_2O, D_2O, and D_2O with a H_2 balloon as the proton source by a tandem reaction to synthesize *cis*-stilbene. (E) Conversion and selectivity for different reaction substrates.

Vis light (Table S13, entry 10) for the same time, the conversions of *trans*-stilbene into *cis*-stilbene were 48% and 6%, respectively. Therefore, UV light was one of the key factors in the production of *cis*-stilbene.

In addition to activity and selectivity, stability is another key parameter to evaluate the performance of catalysts. After three runs of experiments, the conversion of diphenylacetylene was 95%, and the selectivity of

cis-stilbene was 99%, proving that the catalytic activity of **$Co_5Zn_3L_6$** hardly changed (Figure 4C). In PXRD pattern (Figure S52), the Zn 2p and Co 2p XPS spectra (Figure S53) of **$Co_5Zn_3L_6$** after the test matched that before the test, which proved that the structure of **$Co_5Zn_3L_6$** was stable during the catalytic process.

3.5 | Substrate scope

To verify the applicability of this tandem reaction, we have extended the study of various substrates with different functional groups (Figure 4E). Regardless of the substrates with electron-donating groups (–Cl, –Br, $–OCH_3$, and $–NH_2$) or electron-withdrawing groups ($–CF_3$), the conversion rate could reach more than 98% and the selectivity of Z-alkenes was maintained at more than 99%. More importantly, when the substrate was changed to 1-ethoxy-4-[2-(4-methylphenyl)ethynyl]benzene with two different para-substituents, the conversion rate could reach 99% and the selectivity of Z-1-ethoxy-4-(4-methylstylyl)benzene remained above 99%. These results demonstrated the generality and application potential of the photocatalytic tandem reaction of hydrogen evolution and semi-hydrogenation of alkynes.

3.6 | Mechanism of the photocatalytic tandem reaction

The experimental results (Figures 2C and 4B) showed that H_2 would be produced regardless of whether the reaction system included diphenylacetylene or not, so the main intermediate of the separate hydrogen evolution reaction and the tandem reaction was the same Co^{III}–H (the same Step A and Step B).[29,53] However, there were two reaction paths after the catalytic site absorbed *H to form Co^{III}–H: one was the coupling another proton in solution to generate H_2 (Step C of the hydrogen evolution reaction) and the other was the combination of *H and the carbon–carbon triple bond of alkynes to produce intermediate R_1*C=CHR_2 (Step C of the tandem reaction). Taking **$Co_5Zn_3L_6$** as the catalyst model and diphenylacetylene as the substrate, DFT calculations were carried out to understand the catalytic mechanism of the tandem reaction. At the octahedral-coordinated Co site, the ΔG for the formation of H_2 was 0.23 eV, while the ΔG for the formation of Ph*C=CHPh was 0.13 eV (Figure 5A and Table S14). Therefore, the generated *H on the Co active sites preferentially combined with C≡C of diphenylacetylene instead of H_2 release. As shown in Figure 5B, in Step C of the tandem reaction, Co^{III}–H conducted a nucleophilic attack on a triple-bonded carbon atom of an electrophilic alkyne via a π complex to form Co^{III}–R_1C=CHR_2, which further obtained a proton from

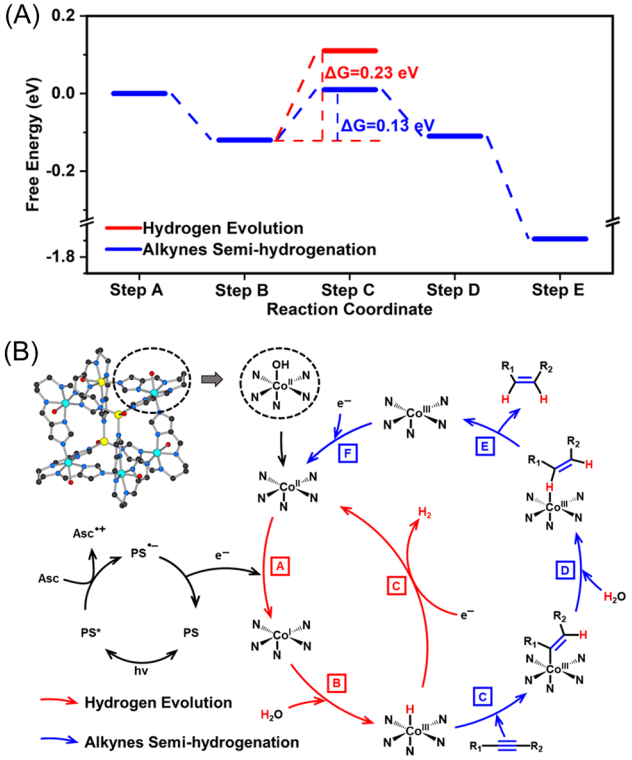

FIGURE 5 (A) Calculated free-energy diagram for the tandem reaction over **$Co_5Zn_3L_6$**. (B) Possible reaction mechanism for the photocatalytic hydrogen evolution and Z-selective alkyne semi-hydrogenation by **$Co_5Zn_3L_6$**. Asc, ascorbic acid; PS, photosensitizer.

H_2O to generate Co^{III}–R_1HC=CHR_2 (Step D, $\Delta G = -0.12$ eV). It is worth noting that the six-coordinated Co catalytic site was at the apex of the cube cage; the entire cage had a steric hindrance effect on the adsorbed Co^{III}–R_1C=CHR_2, so it tended to form a configuration in which two benzene rings were on the same side of the C=C bond away from the cage, resulting in the high selectivity of Z-alkene. In addition, even if a small amount of *trans*-stilbene was produced, it could easily undergo *trans* to *cis* isomerization under full spectrum (including UV light) illumination, resulting in the final production of *cis*-stilbene. In a word, the steric hindrance effect and UV light were two main reasons why that diphenylacetylene was more likely to be reduced to *cis*-stilbene.

In Step E, the ΔG for direct desorption of the alkene was extremely low, being −1.58 eV. Therefore, *cis*-stilbene was prone to scatter from the Co catalytic site, resulting in its inability to further hydrogenate to produce 1,2-diphenylethane. Additionally, we monitored the photocatalytic reaction process through ^{1}H NMR. As shown in Figure S54, before illumination, only diphenylacetylene was present in the reaction system. As the illumination time increased, the diphenylacetylene signals gradually decreased, while the *cis*-stilbene signals

began to appear and gradually increased, without the signals of other products. Moreover, we replaced diphenylacetylene with *cis*-stilbene and performed the reaction under the same conditions. As a result, the product that we obtained was a mixture of *cis* and *trans* isomers of stilbene (*cis*-stilbene: *trans*-stilbene = 98%: 2%), without the production of the hydrogenation product (1,2-diphenylethane). Therefore, both experiments and calculations have proved that the Co catalytic site cannot adsorb and activate *cis*-stilbene, so it will not be further hydrogenated to produce 1,2-diphenylethane.

4 | CONCLUSION

In summary, we designed and synthesized a series of stable MOCs-based photocatalytic hydrogen evolution catalysts, in which **$Co_5Zn_3L_6$** showed high catalytic activity with the H_2 generation rate of 8.81 mmol g^{-1} h^{-1}. The catalytic performance was significantly improved due to the bimetallic synergistic effect, leading to a faster electron transfer rate and higher separation efficiency of photogenerated electrons and holes. More importantly, we successfully photosynthesized Z-olefins using water as the proton source. This tandem reaction strategy showed very high conversion (>98%) and selectivity (>99%), as well as application potential for the synthesis of fine chemicals. Significantly, this work provides a promising route for designing more photoinduced low-cost and energy-efficient tandem reactions to obtain high-value and selective organic products.

ACKNOWLEDGMENTS

This work was financially supported by NSFC (Grant Nos. 92061101, 22271104, 21871141, 22225109, and 21901123), the Excellent Youth Foundation of Jiangsu Scientific Committee (BK20211593), the project funded by the China Postdoctoral Science Foundation (2018M630572), the Priority Academic Program Development of Jiangsu Higher Education Institutions, and the Foundation of Jiangsu Collaborative Innovation Center of Biomedical Functional Materials, the National Key Research and Development Project of China (Grant No. 2021YFC2100100), and the Natural Science Foundation of Jiangsu Province (Grant No. BK20190694). Jia-Ni Lu and Yunze Huang contributed equally to this work.

CONFLICT OF INTEREST STATEMENT

The authors declare no conflict of interest.

ORCID

Ya-Qian Lan http://orcid.org/0000-0002-2140-7980

REFERENCES

1. Kyriakou G, Boucher MB, Jewell AD, et al. Isolated metal atom geometries as a strategy for selective heterogeneous hydrogenations. *Science*. 2012;335(6073):1209-1212.
2. Riley C, Zhou S, Kunwar D, et al. Design of effective catalysts for selective alkyne hydrogenation by doping of ceria with a single-atom promotor. *J Am Chem Soc*. 2018;140(40): 12964-12973.
3. Zhao X, Zhou L, Zhang W, et al. Thiol treatment creates selective palladium catalysts for semihydrogenation of internal alkynes. *Chem*. 2018;4(5):1080-1091.
4. Albani D, Shahrokhi M, Chen Z, et al. Selective ensembles in supported palladium sulfide nanoparticles for alkyne semihydrogenation. *Nat Commun*. 2018;9:2634.
5. Farrar-Tobar RA, Weber S, Csendes Z, et al. E-selective manganese-catalyzed semihydrogenation of alkynes with H_2 directly employed or in situ-generated. *ACS Catal*. 2022;12(4): 2253-2260.
6. Choe K, Zheng F, Wang H, et al. Fast and selective semihydrogenation of alkynes by palladium nanoparticles sandwiched in metal–organic frameworks. *Angew Chem Int Ed*. 2020;59(9):3650-3657.
7. Zhao L, Qin X, Zhang X, et al. A magnetically separable Pd single-atom catalyst for efficient selective hydrogenation of phenylacetylene. *Adv Mater*. 2022;34(20):2110455.
8. Park BY, Lim T, Han MS. A simple and efficient in situ generated copper nanocatalyst for stereoselective semihydrogenation of alkynes. *Chem Commun*. 2021;57(56):6891-6894.
9. Oger C, Balas L, Durand T, Galano J-M. Are alkyne reductions chemo-, regio-, and stereoselective enough to provide pure (Z)-olefins in polyfunctionalized bioactive molecules? *Chem Rev*. 2013;113(3):1313-1350.
10. Lee MT, Goodstein MB, Lalic G. Synthesis of isomerically pure (Z)-alkenes from terminal alkynes and terminal alkenes: silver-catalyzed hydroalkylation of alkynes. *J Am Chem Soc*. 2019;141(43):17086-17091.
11. Bhadra M, Kandambeth S, Sahoo MK, Addicoat M, Balaraman E, Banerjee R. Triazine functionalized porous covalent organic framework for photo-organocatalytic E–Z isomerization of olefins. *J Am Chem Soc*. 2019;141(15): 6152-6156.
12. Jiang R, Ding L, Zheng C, You S-L. Iridium-catalyzed Z-retentive asymmetric allylic substitution reactions. *Science*. 2021;371(6527):380-386.
13. Wang B, Lanterna AE, Scaiano JC. Mechanistic insights on the semihydrogenation of alkynes over different nanostructured photocatalysts. *ACS Catal*. 2021;11(7):4230-4238.
14. Kuwahara Y, Kango H, Yamashita H. Pd nanoparticles and aminopolymers confined in hollow silica spheres as efficient and reusable heterogeneous catalysts for semihydrogenation of alkynes. *ACS Catal*. 2019;9(3):1993-2006.
15. Ji S, Chen Y, Zhao S, et al. Atomically dispersed ruthenium species inside metal–organic frameworks: combining the high activity of atomic sites and the molecular sieving effect of MOFs. *Angew Chem Int Ed*. 2019;58(13):4271-4275.
16. He X, He Q, Deng Y, et al. A versatile route to fabricate single atom catalysts with high chemoselectivity and regioselectivity in hydrogenation. *Nat Commun*. 2019;10:3663.

17. Chernichenko K, Madarász Á, Pápai I, Nieger M, Leskelä M, Repo T. A frustrated-Lewis-pair approach to catalytic reduction of alkynes to *cis*-alkenes. *Nat Chem*. 2013;5(8):718-723.
18. Wan X-K, Wang J-Q, Nan Z-A, Wang Q-M. Ligand effects in catalysis by atomically precise gold nanoclusters. *Sci Adv*. 2017;3(10):e1701823.
19. Zheng W, Zhou Y, Li Y. PVC-NHC-Pd(0): an efficient and reusable heterogeneous catalyst for highly *cis*-selective semihydrogenation of alkynes using formic acid as hydrogen source. *Inorg Chem Commun*. 2021;134:109014.
20. Belger C, Neisius NM, Plietker B. A selective Ru-catalyzed semireduction of alkynes to Z olefins under transfer-hydrogenation conditions. *Chem Eur J*. 2010;16(40):12214-12220.
21. Nie R, Tao Y, Nie Y, et al. Recent advances in catalytic transfer hydrogenation with formic acid over heterogeneous transition metal catalysts. *ACS Catal*. 2021;11(3):1071-1095.
22. Lv H, Qin H, Sun M, Jia F, Huang B, Liu B. Mesoporosity-enabled selectivity of mesoporous palladium-based nanocrystals catalysts in semihydrogenation of alkynes. *Angew Chem Int Ed*. 2021;61(8):e202114539.
23. Fu S, Chen N-Y, Liu X, Shao Z, Luo S-P, Liu Q. Ligand-controlled cobalt-catalyzed transfer hydrogenation of alkynes: stereodivergent synthesis of Z- and E-alkenes. *J Am Chem Soc*. 2016;138(27):8588-8594.
24. Han C, Du L, Konarova M, Qi D-C, Phillips DL, Xu J. Beyond hydrogen evolution: solar-driven, water-donating transfer hydrogenation over platinum/carbon nitride. *ACS Catal*. 2020;10(16):9227-9235.
25. Zhao E, Li M, Xu B, et al. Transfer hydrogenation with a carbon-nitride-supported palladium single-atom photocatalyst and water as a proton source. *Angew Chem Int Ed*. 2022;61(40):e202207410.
26. Yao F, Dai L, Bi J, et al. Loofah-like carbon nitride sponge towards the highly-efficient photocatalytic transfer hydrogenation of nitrophenols with water as the hydrogen source. *Chem Eng J*. 2022;444:136430.
27. Yang Y, Jing X, Zhang J, Yang F, Duan C. Modifying electron injection kinetics for selective photoreduction of nitroarenes into cyclic and asymmetric azo compounds. *Nat Commun*. 2022;13:1940.
28. Li M, Zhang N, Long R, Ye W, Wang C, Xiong Y. PdPt alloy nanocatalysts supported on TiO_2: maneuvering metal–hydrogen interactions for light-driven and water-donating selective alkyne semihydrogenation. *Small*. 2017;13(23):1604173.
29. Arcudi F, Đorđević L, Schweitzer N, Stupp SI, Weiss EA. Selective visible-light photocatalysis of acetylene to ethylene using a cobalt molecular catalyst and water as a proton source. *Nat Chem*. 2022;14(9):1007-1012.
30. Rau S, Schäfer B, Gleich D, et al. A supramolecular photocatalyst for the production of hydrogen and the selective hydrogenation of tolane. *Angew Chem Int Ed*. 2006;45(37):6215-6218.
31. Lu M, Zhang M, Liu J, et al. Covalent organic framework based functional materials: important catalysts for efficient CO_2 utilization. *Angew Chem Int Ed*. 2022;61(15):e202200003.
32. Xia Y-S, Tang M, Zhang L, et al. Tandem utilization of CO_2 photoreduction products for the carbonylation of aryl iodides. *Nat Commun*. 2022;13:2964.
33. Ma X, Liu H, Yang W, Mao G, Zheng L, Jiang H-L. Modulating coordination environment of single-atom catalysts and their proximity to photosensitive units for boosting MOF photocatalysis. *J Am Chem Soc*. 2021;143(31):12220-12229.
34. Kang X-M, Tang M-H, Yang G-L, Zhao B. Cluster/cage-based coordination polymers with tetrazole derivatives. *Coord Chem Rev*. 2020;422:213424.
35. Zhang L, Li X-X, Lang Z-L, et al. Enhanced cuprophilic interactions in crystalline catalysts facilitate the highly selective electroreduction of CO_2 to CH_4. *J Am Chem Soc*. 2021;143(10):3808-3816.
36. Xue Y, Hang X, Ding J, et al. Catalysis within coordination cages. *Coord Chem Rev*. 2021;430:213656.
37. Fan W, Peh SB, Zhang Z, et al. Tetrazole-functionalized zirconium metal-organic cages for efficient C_2H_2/C_2H_4 and C_2H_2/CO_2 separations. *Angew Chem Int Ed*. 2021;60(32):17338-17343.
38. Zhu J-L, Zhang D, Ronson TK, et al. A cavity-tailored metal-organic cage entraps gases selectively in solution and the amorphous solid state. *Angew Chem Int Ed*. 2021;60(21):11789-11792.
39. Luo D, Wang X-Z, Yang C, Zhou X-P, Li D. Self-assembly of chiral metal–organic tetartoid. *J Am Chem Soc*. 2018;140(1):118-121.
40. Tian L, Wang C, Zhao H, et al. Rational approach to plasmonic dimers with controlled gap distance, symmetry, and capability of precisely hosting guest molecules in hotspot regions. *J Am Chem Soc*. 2021;143(23):8631-8638.
41. Tang X, Chu D, Gong W, Cui Y, Liu Y. Metal-organic cages with missing linker defects. *Angew Chem Int Ed*. 2021;60(16):9099-9105.
42. Kieffer M, Bilbeisi RA, Thoburn JD, Clegg JK, Nitschke JR. Guest binding drives host redistribution in libraries of $Co^{II}{}_4L_4$ cages. *Angew Chem Int Ed*. 2020;59(28):11369-11373.
43. Wu K, Li K, Chen S, et al. The redox coupling effect in a photocatalytic Ru^{II}–Pd^{II} cage with TTF guest as electron relay mediator for visible-light hydrogen-evolving promotion. *Angew Chem Int Ed*. 2020;59(7):2639-2643.
44. Tan C, Jiao J, Li Z, Liu Y, Han X, Cui Y. Design and assembly of a chiral metallosalen-based octahedral coordination cage for supramolecular asymmetric catalysis. *Angew Chem Int Ed*. 2018;57(8):2085-2090.
45. Liu G, Zhou M, Su K, Babarao R, Yuan D, Hong M. Stabilizing the extrinsic porosity in metal-organic cages-based supramolecular framework by in situ catalytic polymerization. *CCS Chem*. 2021;3(5):1382-1390.
46. Bodedla GB, Wong W-Y, Zhu X. Coupling of a new porphyrin photosensitizer and cobaloxime cocatalyst for highly efficient photocatalytic H_2 evolution. *J Mater Chem A*. 2021;9(36):20645-20652.
47. Banerjee T, Haase F, Savasci G, Gottschling K, Ochsenfeld C, Lotsch BV. Single-site photocatalytic H_2 evolution from covalent organic frameworks with molecular cobaloxime co-catalysts. *J Am Chem Soc*. 2017;139(45):16228-16234.
48. Huang B, Xiao L, Lu J, Zhuang L. Spatially resolved quantification of the surface reactivity of solid. *Angew Chem Int Ed*. 2016;55(21):6239-6243.
49. Jafarpour M, Feizpour F, Rezaeifard A, Pourmorteza N, Breit B. Tandem photocatalysis protocol for hydrogen generation/olefin hydrogenation using Pd-g-C_3N_4-imine/TiO_2 nanoparticles. *Inorg Chem*. 2021;60(13):9484-9495.

50. Jeske K, Rösler T, Belleflamme M, et al. Back cover: direct conversion of syngas to higher alcohols via tandem integration of Fischer–Tropsch synthesis and reductive hydroformylation. *Angew Chem Int Ed*. 2022;61(31):e202201004.
51. Vermeire FH, Chung Y, Green WH. Predicting solubility limits of organic solutes for a wide range of solvents and temperatures. *J Am Chem Soc*. 2022;144(24):10785-10797.
52. Mellmer MA, Sanpitakseree C, Demir B, et al. Solvent-enabled control of reactivity for liquid-phase reactions of biomass-derived compounds. *Nat Catal*. 2018;1(3):199-207.
53. Gnaim S, Bauer A, Zhang H-J, et al. Cobalt-electrocatalytic HAT for functionalization of unsaturated C–C bonds. *Nature*. 2022;605(7911):687-695.

SUPPORTING INFORMATION

Additional supporting information can be found online in the Supporting Information section at the end of this article.

How to cite this article: Lu J-N, Huang Y, Xia Y-S, et al. Selective photosynthesis of Z-olefins through crystalline metal–organic cage-initiated expeditious cascade reactions. *Carbon Energy*. 2023;e396. doi:10.1002/cey2.396